Biochemistry

 Volume 40, Number 50 December 18, 2001

Current Topics

Dynamics of Excitation Energy Transfer in the LH1 and LH2 Light-Harvesting Complexes of Photosynthetic Bacteria†

Rienk van Grondelle*,‡ and Vladimir Novoderezhkin§

Department of Biophysics and Physics of Complex Systems, Faculty of Sciences, Vrije Universiteit, De Boelelaan 1081, 1081 HV Amsterdam, The Netherlands, and A. N. Belozersky Institute of Physico-Chemical Biology, Moscow State University, Moscow 119899, Russia

Received July 5, 2001; Revised Manuscript Received October 1, 2001

ABSTRACT: Photosynthetic light harvesting is a unique life process that occurs with amazing efficiency. Since the discovery of the structure of the bacterial peripheral light-harvesting complex (LH2), this process has been studied using a variety of advanced laser spectroscopic methods. We are now in a position to discuss the physical origins of excitation energy transfer and trapping in the LH2 and LH1 antennae of photosynthetic purple bacteria. We demonstrate that the time evolution of the state created by the light is determined by the combined action of excitonic pigment−pitment interactions, energetic disorder, and coupling to nuclear motion in a pigment−protein complex. A quantitative fit of experimental data using Redfield theory allowed us to determine the pathways and time scales of exciton and vibrational relaxation and analyze separately different contributions to the measured transient absorption dynamics. Furthermore, these dynamics were observed to be strongly dependent on the excitation wavelength. A numerical fit of this dependence turns out to be extremely critical to a variation of the structure and disorder parameters and, therefore, can be used as a test for different antenna models (disordered ring, elliptical deformations, correlated disorder, etc.). The calculated equilibration dynamics in the exciton basis allow a visualization of the exciton motion using a density matrix picture in real space.

In photosynthesis, excitations created by light absorption in the antenna pigments are efficiently transferred to a reaction center where they are used to drive a charge separation (*1*, *2*). Since the early work of Duysens (*3*), it has been known for instance that in the photosynthetic bacterium *Rhodobacter sphaeroides* photons absorbed by carotenoids are transferred efficiently to bacteriochlorophyll and between the various bacteriochlorophyll forms from those absorbing at higher energies (B800 and B850, where the numbers refer to their near-infrared absorption maxima) to the lowest-energy form, B875, and from thereon to the reaction center (RC).[1] During the 1970s and 1980s, the photosynthetic light-harvesting complexes that perform this

† Support by the Dutch Foundation of Scientific Research (NWO) via the Foundation of Earth and Life Sciences (ALW) and the Russian-Dutch Research Cooperation Program and through the Russian Basic Research Foundation (Grant 99-04-49217) are gratefully acknowledged.

* To whom correspondence should be addressed. Fax: +31-20-4447899. E-mail: rienk@nat.vu.nl.

‡ Vrije Universiteit.

§ Moscow State University.

[1] Abbreviations: BChl, bacteriochlorophyll; Chl, chlorophyll; RC, reaction center; CD, circular dichroism; OD, linear absorption (optical density); 3PEPS, three-pulse photon-echo peak shift; fwhm, full width at half-magnitude; TA, transient absorption; PB, photobleaching; SE, stimulated emission; ESA, excited state absorption; SDA, second-derivative of the absorption spectrum.

10.1021/bi011398u CCC: $20.00
Published on Web 11/22/2001

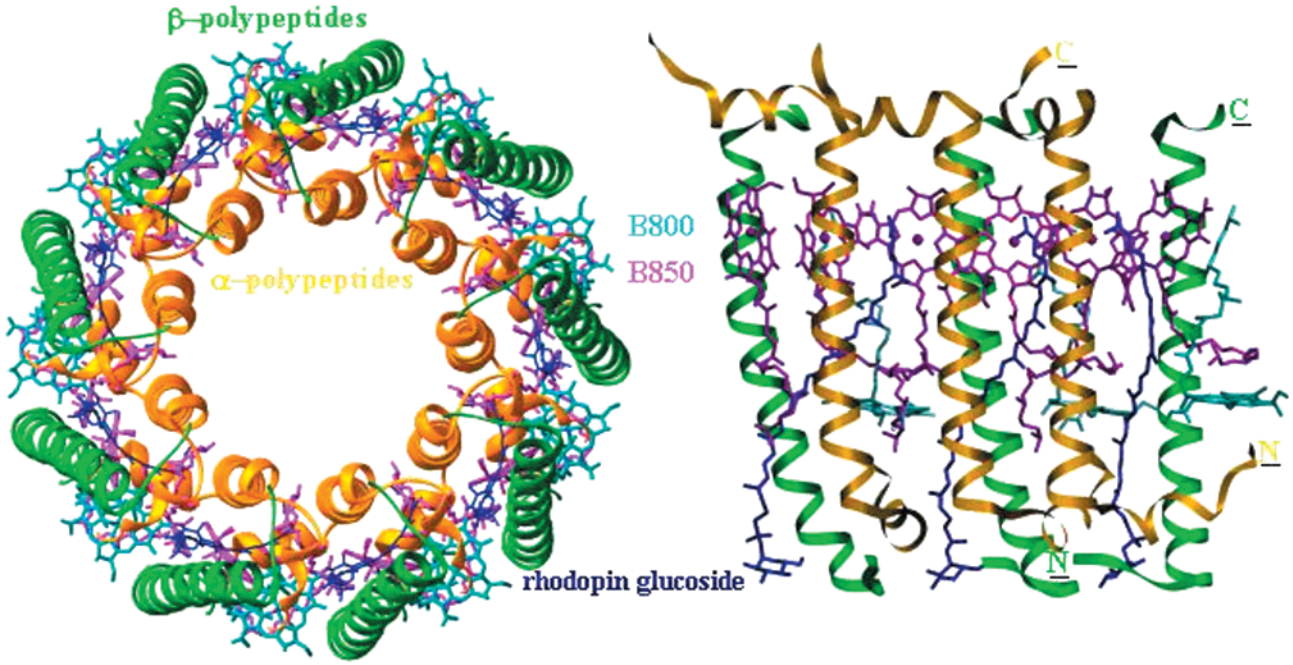

FIGURE 1: Structure of the LH2 complex from *Rps. acidophila* strain 10050. At the left is a top view of the complex looking down in a direction normal to the presumed plane of the photosynthetic membrane: green, β-polypeptides; gold, α-polypeptides; cyan, B800 bacteriochlorophylls; purple, B850 bacteriochlorophylls; and blue, carotenoid rhodopin glucoside. At the right is a side view of a section of the complex. The N- and C-termini of the polypeptides are labeled. This view clearly shows the organization of the light-absorbing pigments. This figure was kindly produced by T. Howard (Glasgow University, Glasgow, Scotland).

process were obtained in pure form (see ref *4* for a review), and this led to a large variety of spectroscopic studies and attempts to obtain structural data (for a review, see ref *5*). Only in 1995 was the structure of the peripheral light-harvesting complex of the photosynthetic bacterium *Rhodopseudomonas acidophila* obtained to atomic resolution (*6*), a year later followed by the structure of the LH2 antenna of *Rhodospirillum molischianum* (*7*). Although so far no high-resolution structure of the LH1−RC core is available, accurate models have been proposed (*8*−*14*), for a very large part based on the 8 Å density map published for LH1 of *Rhodospirillum rubrum* (*8*). These structures have led to a true explosion of spectroscopic studies of the energy transfer dynamics and attempts to model the relevant phenomenology on the basis of the essential physics (*15*−*56*). In this paper, we will attempt to illustrate our own understanding of how electronic excitations move through LH2 and LH1 on their way to being trapped by the RC and we will develop an intuitive view of excited state relaxation and energy migration in these photosysnthetic systems, where pigment−pigment coupling, energetic disorder, and temperature are all of similar magnitude.

Structure of LH1 and LH2

LH2 of *Rps. acidophila* is an intrinsic membrane protein that is composed of two concentric rings of nine α-polypeptides (inside) and nine β-polypeptides (outside) sandwiched around a ring of 18 strongly coupled bacteriochlorophylls (BChls), which absorbs at ∼850 nm (see Figure 1). The major structural element in both the α- and β-polypeptides consists of a single α-helical transmembrane region, with a highly conserved histidine residue located about one-third of the way across from the periplasmic side of the membrane. These histidines function as the ligands for the 18 BChls, which have their chlorin plane more or less parallel to the C_9 symmetry axis and their Q_y almost in the plane of the membrane (*6*, *7*, *57*−*59*). When the B850 ring is viewed as a ring of BChl dimers, with each dimer associated with one pair of αβ-polypeptides, the intradimer center-to-center distance between the BChls is ∼9 Å, which is in fact very similar to the interdimer distance. The electronic coupling between the neighboring BChls has been estimated from calculations (*30*, *32*, *33*, *46*, *55*, *56*) and experiments (*19*, *24*, *44*, *49*, *60*, *61*) to be ∼300 cm^{-1} for the intradimer pair and slightly less for the interdimer pair. In LH2 of *Rps. acidophila*, a second ring is present, absorbing at 800 nm with the nine BChls positioned between the cytoplasmic end of the β-helices at a nearest-neighbor distance of ∼2 nm. These BChls have their chlorin planes parallel to the membrane plane (*6*, *7*, *57*−*59*), and they are only weakly coupled both to their nearest neighbors (30 cm^{-1}) and to the BChls in the B850 ring (*30*, *54*−*56*).

For LH1, only low-resolution structures are available. These strongly suggest that the isolated complex is an $(\alpha\beta)_{16}BChl_{32}$ aggregate in which the ring of 32 BChls is structurally very similar to the ring of 18 strongly coupled BChls in LH2. LH1 can be reversibly dissociated using detergents into $(\alpha\beta)BChl_2$ subunits, called B820, that display a maximum absorption at 820 nm (*60*−*62*). The major reason for this is that the major interactions that stabilize LH1 in fact occur within such $(\alpha\beta)BChl_2$ subunits; this is in contrast to LH2 where H-bonds exist between amino acids and BChls in adjacent subunits. In vivo, the LH1 ring is generally not full and probably contains the nonpigmented pufX protein that provides a gate for the reduced quinol to leave the RC and find the cytochrome bc_1 complex (*63*, *64*). It has been demonstrated that in the absence of LH2 and in the presence of PufX the LH1−RC complex occurs as a dimer (*65*), with the dimers arranged in some highly regular fashion in the membrane (*13*, *14*).

Steady State Spectroscopic Properties of LH1 and LH2

In the bacterial antenna complexes, significant excitonic interactions occur between the pigments and these interactions, in combination with exciton−vibration coupling and energetic disorder, both static and dynamic, result in a nonhomogeneous structure of the major near-infrared absorption band. This was for the first time established in experiments where the fluorescence polarization was recorded as a function of the excitation wavelength (*66*, *67*). For LH1, it was observed that excitation in the blue or central part of the band gave slightly positively polarized emission, while the level of polarization increased sharply upon excitation into the red edge. For LH2, the experimental data were very similar with the exception that a minimum or even negative polarization was observed upon excitation in the middle of the band (*68*). For LH1, the shape of the curve was originally explained by Van Mourik et al. (*67*) using a model that assumed energy transfer among a cluster of weakly coupled, energetically disordered pigments. The model was later extended to include excitonic contributions (*51*, *69*). The difference between LH2 and LH1 could be nicely explained by the fact that LH2 displays a much narrower phonon wing due to which in LH2 in the middle of the absorption band more selective excitation of the exciton component that is orthogonal to the emission occurs (*51*). These results were corroborated by spectral hole-burning experiments performed by Small and co-workers (*25*, *70*−*72*).

LH2s typically exhibit intense quasi-conservative CD spectra in the 850 nm region combined with a weak negative transition at ∼780 nm that originates from the B850 excitonic manifold. On top of these features, a CD signal due to the B800 band that varies strongly among the different LH2 complexes can usually be observed (*23*, *24*, *73*). One conspicuous feature is the shift of the zero crossing of the conservative CD relative to the OD maximum. A detailed modeling of these spectra (*23*, *24*, *52*) showed that understanding the observed CD spectrum required at least a large part of the complete ring. The coupling strength was estimated to be ∼300 cm^{-1}, while furthermore, to describe the shape of the observed CD spectrum, an energy difference between the α- and β-bound BChl of 300 cm^{-1} had to be assumed, with the α-bound Bchl higher in energy. Thus, excitonic effects are clearly present in the LH2 spectra, and one might wonder about the extent to which the spectra are truly excitonic. A straightforward calculation splits the degenerate local excited states of the *Rps. acidophila* LH2 ring into eight pairs of doubly degenerate states, while the states at the bottom and top of the excitonic band are single. With the dipoles oriented almost in the plane of the ring, the lowest state, labeled $k = 0$, is optically forbidden, while by far most of the oscillator strength is concentrated in the next two degenerate and orthogonally polarized states, labeled $k = \pm 1$. The hole-burning experiments by Small and co-workers mentioned above (*25*, *26*, *70*−*72*) were interpreted in terms of such an excitonic manifold underlying the broad absorption of LH2. Single-molecule fluorescence excitation experiments by van Oijen et al. (*48*−*50*) were interpreted in terms of the two allowed and orthogonally polarized $k = \pm 1$ states and an almost forbidden $k = 0$ state.

However, although all the molecules in the strongly coupled ring are involved in excitonic interactions, the energy transfer dynamics would generally be determined by an effective delocalization size that can be much smaller than the whole ring due to (i) superposition of several exciton states at thermal equilibrium, (ii) spectral disorder giving rise to nonuniform eigenfunctions, and (iii) dynamic disorder giving rise to polaron formation. For example, even in the case of a spectrally homogeneous LH1 or LH2 antenna (when the exciton eigenfunctions are completely delocalized, i.e., $N_{eig} = 32$ or 18/16), the coherence length of the equilibrated wave packet (N_{coh}) would be 7−9 due to superposition of exciton states populated at room temperature, i.e., significantly smaller than the size of a whole ring. In the presence of the spectral disorder (comparable with the exciton bandwidth), both N_{eig} and N_{coh} values would be significantly decreased.

There is experimental evidence for such a strong disorder in the LH1 and LH2 antennae giving rise to localization on a (small) subset of the total ring, in contrast to the fully delocalized "excitonic" picture. In the perfect exciton view, the lowest electronic state of the ring is almost forbidden for symmetry reasons; consequently, at very low temperatures, LH1 and LH2 would be dark, while at temperatures that approximately match the energy difference between the $k = 0$ and $k = \pm 1$ states, the system would become strongly radiative. However, in reality at 4 K both LH1 and LH2 are rather fluorescent, and for instance, the radiative rate of LH2 is about that of two to three BChl monomers (*34*). Moreover, this radiative rate is close to being independent of temperature. A straightforward calculation shows that this is indeed the case when the stochastic variation in transition frequencies of the individual BChls in the ring (diagonal disorder) is of the same order of magnitude or larger than the coupling. This amount of disorder would significantly decrease the length of the exciton eigenfunctions, N_{eig}. A similar amount of disorder was estimated for a variety of LH1s and LH2s from the modeling of the equilibrated pump−probe spectra of LH2 and LH1 (*31*, *37*, *38*, *43*) or comparing the nonlinear response of the LH2 antenna with that of the B820 subunit (*44*). This latter experiment showed significant differences in the shape and amplitude of the pump−probe spectra of LH2 and B820, reflecting a different degree of exciton delocalization for the whole antenna and the dimeric subunit. Finally, changes in the linear spectra induced by dissociating the LH1 ring into a set of fragments with an increasing number of missing (αβ)$BChl_2$ subunits (*69*) or gradually substituting BChl for BPheo (*51*) also yielded disorder values that exceeded the size of the coupling. Thus, modeling of the LH1 and LH2 antennas with the presence of static disorder together with a weak exciton−phonon coupling yielded N_{eig} values such as 5−11 (*16*, *31*, *32*, *43*, *44*) and N_{coh} values such as 4−6 (*37*, *43*, *44*) at room temperature.

The presence of strong exciton−phonon coupling would give rise to an even further reduction in the exciton size if the phonon-induced length (polaron size) is smaller than the disorder-induced length (*75*, *76*).

In this paper, we will focus the discussion on our own results obtained with the LH1 antenna of *Rhodopseudomonas viridis* (*39*, *43*, *47*, *77*). The elementary subunit of the core antenna of *Rps. viridis* consists of three transmembrane polypeptides, α, β, and γ (*78*). The α- and β-polypeptides,

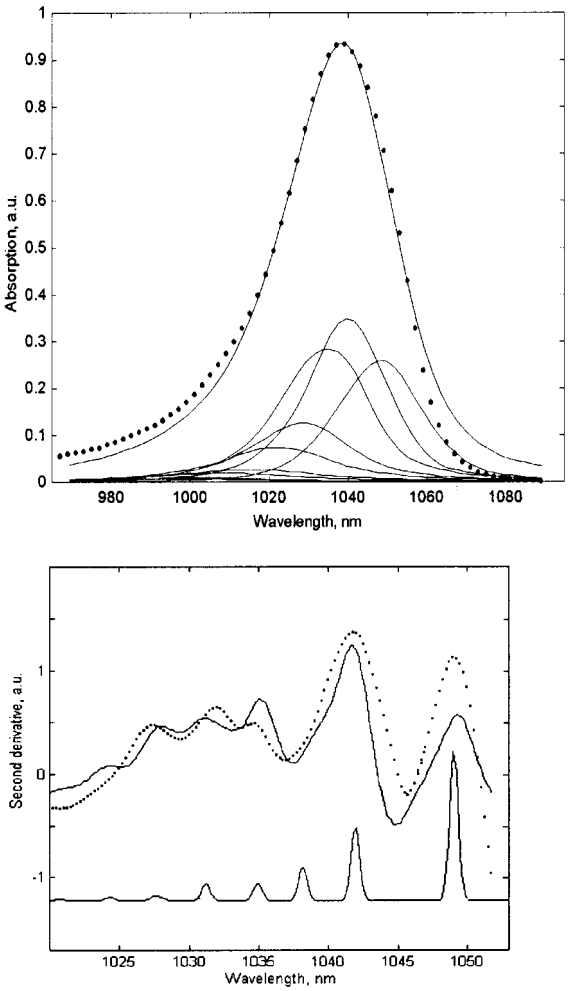

FIGURE 2: Linear absorption at 77 K (top) and the inverted second derivative of the absorption spectrum (SDA) at 4 K (bottom) for the LH1 antenna of *Rps. viridis*. Experimental data are shown as points and calculated data as solid lines. The calculated absorption profile (see Fine Structure of the Absorption Spectrum) is shown together with contributions of the individual exciton components (top). The spectrum of the lowest exciton state without inhomogeneous and homogeneous broadening is also shown in the bottom panel below the SDA spectrum. The 77 K spectrum was calculated using the Redfield theory with the electronic relaxation parameters $\chi = 490$ cm^{-1}, $\Gamma = 70$ cm^{-1}, and $\omega_c = 75$ cm^{-1}, the parameters of two vibrational modes $\Omega_1 = 58$ cm^{-1}, $\Omega_2 = 110$ cm^{-1}, $S_1 = 0.41$, $S_2 = 0.23$, $\gamma_1 = 11$ cm^{-1}, and $\gamma_2 = 11$ cm^{-1}, and the site inhomogeneity $\sigma = 575$ cm^{-1}. At 4 K, we assumed Gaussian line shapes with a fwhm of 4 cm^{-1} for the lowest and 45 cm^{-1} for the higher exciton states. The vibrational parameters are as follows: $\Omega_1 = 65$ cm^{-1}, $\Omega_2 = 101$ cm^{-1}, $S_1 = 0.45$, $S_2 = 0.18$, $\gamma_1 = 7$ cm^{-1}, and $\gamma_2 = 10$ cm^{-1}; the site inhomogeneity $\sigma = 380$ cm^{-1}. The geometry of LH1 (circular aggregate with 32 molecules) and intermolecular couplings ($V_{12} = 400$ cm^{-1} and $V_{23} = 290$ cm^{-1}) were taken to be the same at 77 and 4 K.

binding one BChl molecule each, are analogous to the LH1 proteins found in BChl *a*-containing bacteria. The γ-polypeptide probably does not bind BChl (*78*). At low temperatures, this LH1 displays a spectrum that has a maximum at 1020 nm and exhibits pronounced fine structure (*77*). The details of this fine structure originate from a combination of excitonic interaction among the pigments, the coupling of the excitonic manifold to two low-frequency vibrations, static disorder, and relaxation processes taking place among the excitonic states (see Fine Structure of the Absorption Spectrum for a detailed discussion). Figure 2, which explains this linear absorption spectrum assuming that LH1 is a ring, shows how the various exciton-vibrational levels contribute to the low-temperature absorption spectrum. One discerns three prominent levels, among which is the lowest exciton state. Furthermore, many higher levels have acquired some oscillator strength, largely induced by the diagonal disorder. Recently, it has been proposed that LH2 of *Rps. acidophila* may be elliptically deformed (*48*−*50*). This was based on the relatively large energetic separation (∼120 cm^{-1}) between the two strongest and orthogonally polarized transitions observed in single-molecule fluorescence excitation experiments. We note that in the simulation shown here this separation is ∼70−80 cm^{-1} for LH1. We will argue below that such an elliptical deformation together with relatively low disorder values cannot explain the spectral and dynamic properties of LH1 of *Rps. viridis.* Although in *Rps. viridis* some of these spectral effects (fine structure in the absorption spectrum, oscillatory features in the pump−probe signals) are remarkably strong, we do believe that our description is generally applicable to all bacterial LHs.

Excited State Dynamics of the Bacterial Photosynthetic Light-Harvesting Antenna

As discussed above, the combination of excitonic contributions and disorder makes the linear absorption properties of LH1 and LH2 heterogeneous. As a consequence, following excitation with a short laser pulse, fast relaxation and/or energy migration will occur that generates specific changes in the absorption spectrum with time, which are characteristic for ringlike aggregates such as LH1 and LH2, but that will be absent in, for instance, the dimeric subunit B820 or in monomeric BChl. This was demonstrated for the first time by Visser et al. (*79*), who compared the isotropic transient absorption dynamics observed for LH1 of *Rs. rubrum* with similar experiments on the B820 subunit. For LH1, they observed pronounced dynamics in the transient absorption difference spectrum, a 12 nm red shift of the zero crossing and an 8 nm red shift of the bleaching peak, whereas no such red shift dynamics were observed in the transient absorption spectrum of the B820 subunit as well as for monomeric BChl. Visser et al. explained their results in terms of an ultrafast hopping of the excitation in an energetically disordered antenna. A similar dynamic red shift of ∼20 nm was observed in LH1 of *Rps. capsulatus* (*80*) and in this case ascribed to exciton relaxation. However, the time resolution of both experiments (200−400 fs) was probably not sufficient for a precise estimation of the relaxation and/or hopping time constants.

A pump−probe study employing 35 fs pulses on LH2 of *Rb. sphaeroides* revealed ultrafast relaxation components in the 10−100 fs range (*21*). Similarly, using 40−50 fs pulses in one-color pump−probe experiments on LH1 and LH2 gave a 50−60 fs isotropic decay component, whereas tuning the laser to the blue side of the major absorption band resulted in the appearance of very short-lived (<20 fs) components (*38*, *81*). It is, however, difficult to make any specific assignment of these ultrafast relaxation events since these short pulses essentially excite and probe the total band and have little spectral selectivity. Obtaining transient absorption dynamics that indeed reflect the exciton equilibration with selective excitation and probing would require two-color experiments with longer pulses. Such experiments with

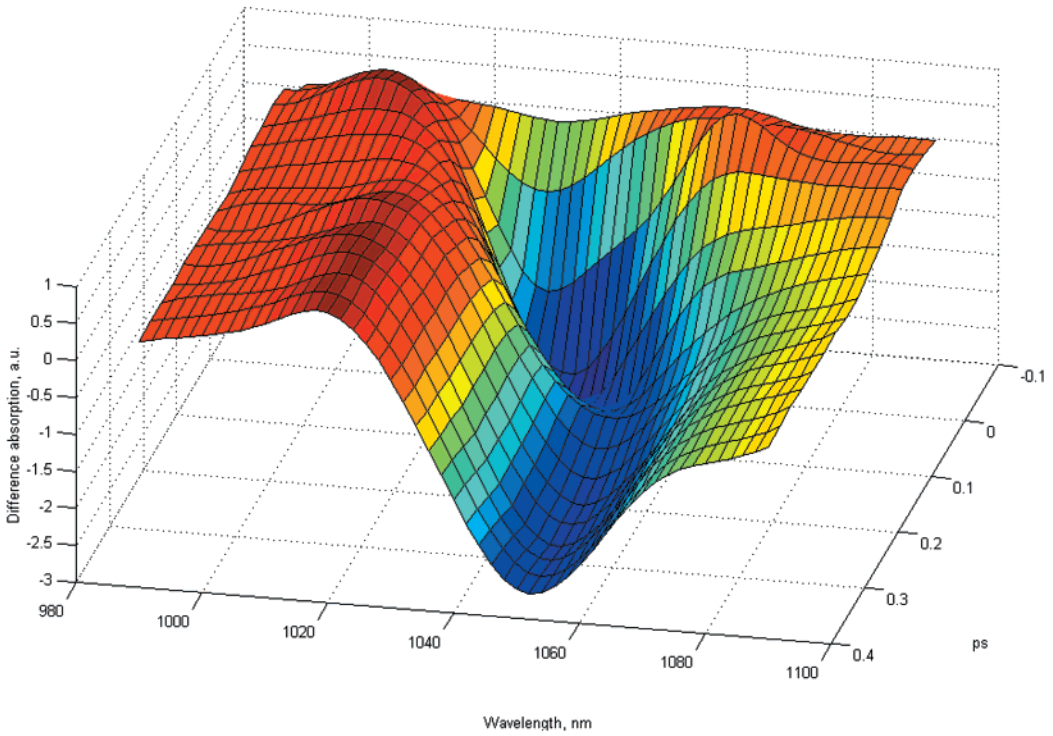

FIGURE 3: Transient absorption spectra measured for the core antenna of *Rps. viridis* at 77 K upon blue side excitation (1017 nm). The pulse duration is 100 fs, and pump−probe delays from −100 to 400 fs are shown (data taken from ref *39*).

longer pulses (65−70 fs) were performed on LH2 of *Rb. sphaeroides* at low temperatures by Vulto et al. (*40*) and at room temperature by Nagarajan et al. (*22*). Both experiments employed "blue" and "red" excitation of the B850 band. Following the blue excitation, a small, 3−5 nm, red shift with a time constant of ∼100 fs was present in both experiments, while this shift was virtually absent upon red excitation. These spectral evolutions were ascribed to relaxation dynamics from higher exciton states initially excited by the short laser pulse.

Very similar two-color pump−probe experiments using <100 fs laser pulses were performed by Monshouwer et al. (*39*) on the LH1 antenna of *Rps. viridis*. Blue side excitation resulted in a dynamic red shift of ∼130−150 fs (see Figure 3). The amplitude of this shift (15−20 nm) is several times larger than that observed for LH2 and is similar to the amplitudes of the red shifts observed in earlier experiments on LH1 (*79*, *80*). When the excitation was tuned to the center of the band, the red shift became less pronounced. In addition to these ultrafast relaxation phenomena, pronounced long-lived oscillatory features (on a time scale of 1−2 ps) were observed for LH1 of *Rps. viridis*, which are ascribed to the coupling of the electronic excitations to two vibrational modes with frequencies of ∼50−60 and 100−110 cm^{-1}.

Apart from a multitude of pump−probe experiments, a few other techniques were applied to study the excited state dynamics in LH1 and LH2. Bradforth et al. (*15*) measured the excited state dynamics in LH1 of *Rb. sphaeroides* by polarized fluorescence upconversion. Their anisotropy decays reflecting exciton equilibration were multiphasic with 100 and 400 fs components being most prominent on the ultrafast time scale. Similar fluorescence upconversion experiments on LH2 gave a slightly faster decay (*16*). Long-lived vibrational coherences in the LH1 and LH2 antennae were studied by femtosecond pump−probe (*82*−*84*), fluorescence upconversion (*15*), transient grating (*17*, *18*), and three-pulse photon-echo peak-shift (3PEPS) experiments (*18*, *85*). The 3PEPS experiments also revealed the time scale of energy transfer by comparison with the B820 subunit (*86*). The peak-shift decay for LH1 and LH2 exhibited a distinct phase (100 fs for LH1 and 70 fs for LH2) that was absent in the B820 subunit and thus was interpreted as being due to energy transfer and/or relaxation in the ring.

Relaxation in the Exciton Manifold

In a series of papers (*43*, *47*, *87*), we have shown that the linear absorption and steady state pump−probe spectra for LH1 of *Rps. viridis* can be quantitatively explained using an exciton approach with a large amount of spectral disorder ("disordered exciton model"). Within the framework of this model, the ultrafast equilibration observed in pump−probe experiments should be ascribed to the relaxation among the states in the one-exciton manifold. To obtain a quantitative explanation of the data for LH1 of *Rps. viridis*, we dressed the exciton model with static disorder, added strong coupling to two vibrational modes, and introduced a weak coupling of the vibrational and electronic coordinates to a thermal bath. To describe the coupled exciton-vibrational dynamics, the Redfield relaxation theory was applied. In this approach, one allows electronic and vibrational coherences in the density matrix to be transferred or to decay via the following set of events schematically summarized in Figure 4.

Generally, the pump pulse creates an excited state in the one-exciton manifold and a hole in the ground state. The excited state consists of exciton-vibrational populations $|k,b\rangle\langle k,b|$ and coherences $|k',b'\rangle\langle k,b|$, where the index b corresponds to a vibronic sublevel of the kth exciton state. In ref *87*, the Redfield tensor was calculated for the case in which all the exciton states have the same oscillator displacement (as shown in Figure 4). In the secular ap-

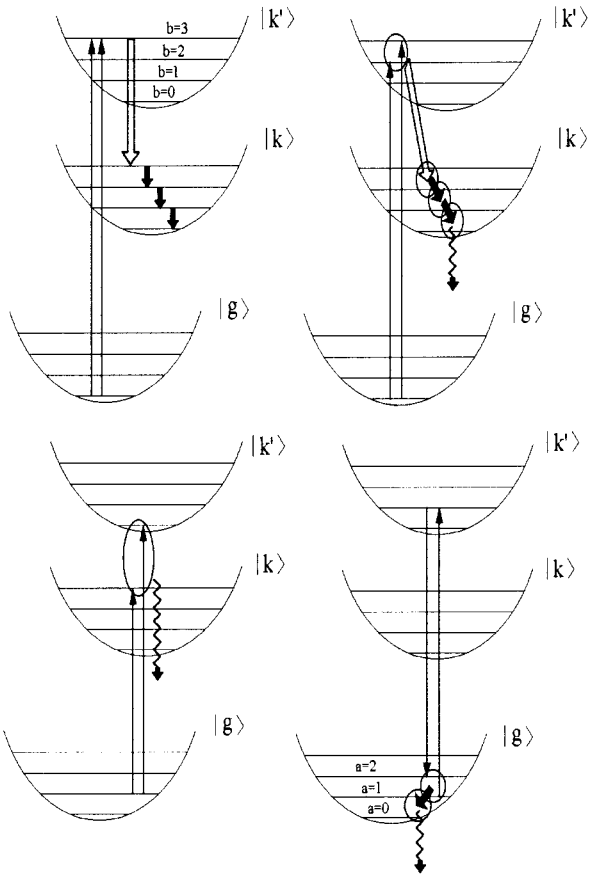

FIGURE 4: Pathways of exciton-vibrational relaxation within the one-exciton manifold in the secular approximation. The ground $|g\rangle$ and two different one-exciton states $|k\rangle$ and $|k'\rangle$ with their vibronic sublevels $a = 0$, 1, 2, or 3 and $b = 0$, 1, 2, or 3 are shown. Thin arrows denote interaction with the pump, and thick white and black arrows correspond to exciton and vibrational relaxation, respectively. Circles symbolize a coherence between two exciton-vibrational states, and zigzag arrows imply a decay of these coherences. At the top left is shown fast relaxation of the exciton population followed by a slower relaxation of vibrational populations (ladder-type one-phonon relaxation induced by linear coupling of the vibrational coordinate with the bath). At the top right are shown two interactions with the pump that create a coherence between two vibronic sublevels (for example, $b = 2$ and $b = 3$) of the higher exciton state. Fast $|k'\rangle \rightarrow |k\rangle$ relaxation does not destroy this coherence. The subsequent vibrational dynamics includes the transfer of coherence (for example, $|b = 2\rangle\langle b = 3| \rightarrow |b = 1\rangle\langle b = 2|$ in the case of linear coupling) and coherence decay. At the bottom left is shown the decay of coherence $|k',b = 0\rangle\langle k,b = 3|$ between two exciton states. In this case, the exciton coherence transfer is nonsecular due to the anharmonicity of the exciton states. The vibrational coherence transfer (for example, to $|k',b = 1\rangle\langle k,b = 4|$) is slow on the time scale of the exciton coherence decay. At the bottom right are shown two interactions with the pump that create a coherence between the $a = 1$ and $a = 2$ sublevels of the ground state. The subsequent dynamics are determined by coherence transfer and decay (similarly, vibrational populations in the ground state can be created with subsequent relaxation).

proximation, the dynamics of populations and coherences are decoupled, and the transfer of coherence only occurs between pairs of states with the same energy difference. For example, the coherence $|k,b_i\rangle\langle k',b_j|$ can be coupled to the coherence $|k,b_{i+s}\rangle\langle k',b_{j+s}|$, where $s = \pm 1$ for one-phonon processes due to linear (i.e., in the vibrational coordinate) system−bath coupling, $s = \pm 2$ for two-phonon processes due to quadratic coupling, etc. In the case of harmonic potentials with equidistant vibrational states, such a coherence transfer would be resonant. In contrast, the coherence between different one-exciton states cannot be transferred due to the "anharmonicity" of the exciton states (in combination with the disorder-induced shift). Typically, exciton relaxation is much faster than the vibrational dynamics, and does not destroy the vibrational coherence, as was demonstrated for LH1 (*39*), the chlorosomal antenna (*88*), and the special pair of the reaction center (*89*, *90*). Figure 4 shows the relaxation pathways in the secular approximation, i.e. population relaxation (top left frame), vibrational coherence transfer superimposed on exciton relaxation (top right), and exciton coherence decay (bottom left). The dynamics of the ground state include vibrational equilibration, i.e., relaxation of populations and coherence transfer and decay processes (Figure 4, bottom right). The nonsecular terms (responsible for nonresonant coherence transfer, including the coupling between populations and coherences) make relatively small but non-zero contributions to the time evolution of the density matrix. The Redfield theory has been used to study vibrational relaxation in the bacterial reaction center (*91*, *92*), exciton relaxation in LH2 (*37*, *93*) and molecular aggregates (*94*, *95*), coupled exciton-vibrational relaxation in Chl *a*−Chl *b* heterodimers of LHC-II (*96*, *97*), and exciton-vibrational relaxation in LH1 (*47*, *87*).

As in previous studies, we assume that the pigment arrangement in the core antenna of *Rps. viridis* is analogous to that of the BChl *a*-containing bacteria. As a model of the antenna, we consider a circular aggregate of 32 BChl *b* molecules with C_{16} symmetry (the elementary unit cell contains two BChl *b* molecules, bound to the α- and β-polypeptides). The orientations of the two BChls in a dimeric unit cell and the Mg−Mg distances between BChls are essentially the same as those for the strongly coupled B850 ring of BChl *a*'s in the LH2 antenna from *Rps. acidophila* (*6*). The intra- and interdimer interaction energies are as follows: $V_{12} = 400$ cm^{-1} and $V_{23} = 290$ cm^{-1}, respectively. The site inhomogeneity of the LH1 antenna was modeled by uncorrelated diagonal disorder with a width σ of 575 cm^{-1} (fwhm). Alternative models with correlated disorder, elliptic deformation of the ring, and/or breaking of the closed ring by removal of a few dimeric subunits were analyzed as well.

In LH1 of *Rps. viridis*, strong oscillatory features are observed in the pump−probe signals (*39*). To match these data to the calculated spectra and dynamics, we have assumed that the electronic transitions are coupled to two vibrational modes with frequencies Ω_1 and Ω_2 of 58 and 110 cm^{-1}, respectively, Huang−Rhys factors S_1 and S_2 of 0.41 and 0.23, respectively, and relaxation rate constants (i.e., the rates for the $1 \rightarrow 0$ vibronic transition) γ_1 and γ_2 of 11 cm^{-1} at 77 K (*47*). In the Redfield approach, the important parameter that governs the relaxation down the one-exciton manifold is the spectral density of the system−bath coupling. This spectral density determines the degree to which two levels are connected. It turns out that with a characteristic frequency ω_c of 75 cm^{-1} we obtain the best fit to the experimental data. This value implies that relaxation from a certain exciton level occurs mainly to the next two or three levels below it. The pure dephasing (Γ) that contributes (together with population relaxation) to the homogeneous broadening of

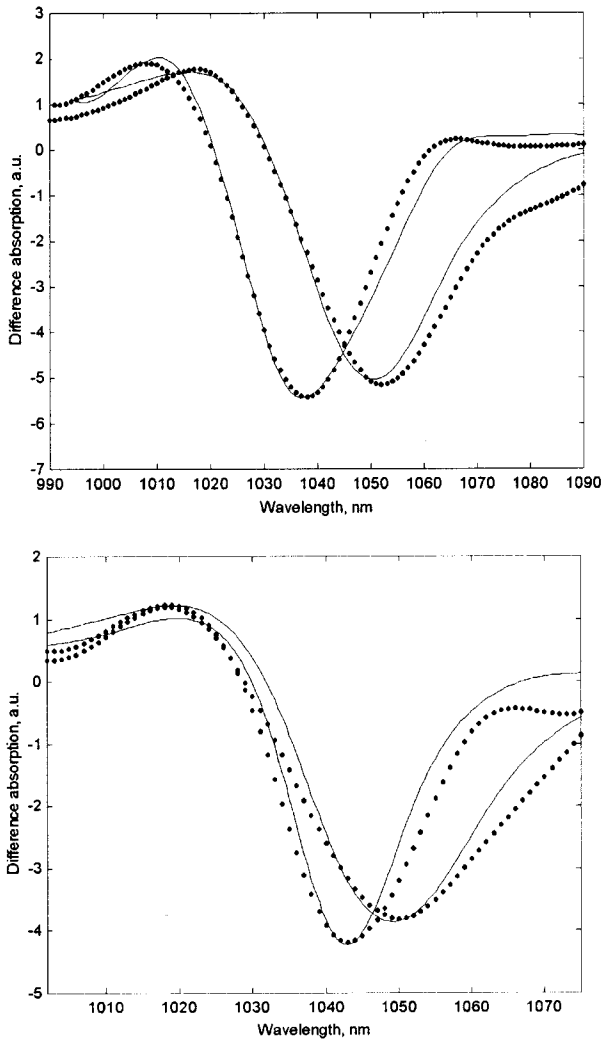

FIGURE 5: Experimental (points) and calculated (solid lines) pump−probe spectra upon 1017 nm excitation (top) and 1036 nm excitation (bottom) for the LH1 antenna of *Rps. viridis* at 77 K. The spectra are shown after delays of 0 and 400 fs (note that an increase in the time delay corresponds to a red shift of the spectra). The calculated spectra were obtained using the same parameters as those for the linear absorption fit at 77 K (see Figure 2).

each of the exciton levels is equal to 70 cm^{-1}. The dynamic disorder value χ (amplitude of the site energy modulation) required to explain the experimental relaxation dynamics is equal to 350−500 cm^{-1}. In the case of uncorrelated diagonal coupling (i.e., the fluctuations of the different site energies are uncorrelated), the coupling strength in the eigenstate representation χ_{eig} would be related to χ through the fourth power of the wave function amplitude (*95*). The latter is equal to the participation ratio N_{eig}^{-1} which is ∼0.1 for the higher exciton states in our model (*43*). Thus, the fluctuations that induce relaxation from the higher states are relatively weak in the eigenstate representation, and consequently, the Redfield approximation is valid (at room temperature and even lower temperatures up to 77 K).

This model allowed us to obtain a quantitative fit of the experimental data, including absorption and pump−probe transient absorption (TA) spectra for the core antenna of *Rps. viridis* at 77 K (*39*). Figure 5 shows a fit of the isotropic TA spectra for two different excitation wavelengths, corresponding to the blue side and the middle of the band (1017 and 1036 nm, respectively). The TA spectra are shown (both measured and calculated) with a delay of 0 fs, corresponding to maximal pump−probe overlap, and a delay of 400 fs when the exciton relaxation is complete (the largest part of the dynamic red shift occurs at delays between −100 and 250 fs). Upon blue side excitation, the experimental spectrum exhibits an 11 nm shift of the ESA maximum, a 10 nm shift of the isosbestic point, and a 15 nm shift of the bleaching maximum. Upon middle-band excitation, there is no shift of the ESA maximum or the isosbestic point, whereas the bleaching peak shifts to the red by 7 nm. Note that these values are reproduced by our model with an accuracy of ∼2 nm (Figure 5).

More detailed calculations have shown that during delays between −100 and 130 fs the TA dynamics are strongly influenced by the superposition of a sequential (true pump−probe) signal and what is typically called the coherent artifact, resulting from a reversal in time of the pump and probe fields during their overlap. For instance, for 1017 nm excitation, the sequential signal is responsible for the bleaching peak that is continuously shifting due to exciton relaxation from 1044 to 1050 nm between −100 and 230 fs delays. In contrast, the coherent artifact signal has a negative peak at 1036 nm that reaches its maximal value near zero delay and completely disappears after 130 fs. The combined action of these sequential and coherent factors results in the very large apparent Stokes shift of the total signal from 1036 to 1050 nm at delays between −100 and 230 fs.

For larger delays (from 400 fs to 2 ps), the calculated and measured spectra show no more dynamics, such as a further red shift or some changes in line shape. The vibrational coherence persists up to 1.5−2 ps, giving rise to some oscillations in the bleaching peak position (within 1−2 nm) and in the bleaching amplitude (within ±5% of this amplitude). However, the vibrational population dynamics contribute only weakly (less than 1 nm) to the dynamic red shift. It thus is clear that the TA shifting during the first 100−200 fs is determined mostly by exciton relaxation.

Upon middle-band excitation, there is no pronounced red shift dynamics of the sequential signal, and in that case, the TA evolution is determined mostly by the coherent contribution. The latter has a negative peak at 1043 nm giving rise to the TA shifting from 1043 to 1050 nm (as shown in Figure 5, bottom frame).

In our model, downhill transfer between pairs of one-exciton levels occurs in the time range of 50−150 fs. The lifetime of the *k*th level (determined by the sum of the downhill transfer rates) decreases rapidly with *k*. For the six lowest exciton states, these lifetimes are approximately (in increasing order of energy level): 250, 75, 40, 25, 20, and 12 fs. Thus, the lifetimes of the higher states are significantly shorter than the pulse duration (100 fs), but we cannot use shorter pulses to obtain a direct visualization of this fast relaxation because under broad-band excitation it would be impossible to selectively excite higher levels. That is why these true relaxation components are always hidden under the more slow pulse envelope. Moreover, they are also masked by the coherent artifact inducing an additional decay component. The latter has a time constant that is approximately $\sqrt{2}$ times larger than the pulse duration, i.e., 100−150 fs, that has often been interpreted as the "main relaxation component".

Uncorrelated Disorder versus Correlated Distortion of the Ring

It is important to notice that the excitation wavelength-dependent TA shift (shown in Figure 5) is extremely sensitive to the exciton structure of the absorption band, and therefore can be used as a test for different antenna models. For example, in the disordered exciton model, we used a large disorder value ($\sigma/V_{12} = 1.4$) to obtain the splitting value necessary to explain the experimentally observed absorption profile. Satisfactory fits can also be obtained using alternative sets of interaction energies with a V_{12} of 260−600 cm^{-1} and a σ/V_{12} of 0.8−1.6 (*43*). This gave a delocalization size N_{coh} of 5−10 at 77 K and 4−6 at room temperature.

In principle, the steady state spectra can be modeled using an alternative parameter set with higher σ/V_{12} and lower χ and Γ values. For example, Kühn and Sundström (*37*) explained the steady state pump−probe spectrum for LH2 supposing $\sigma/V_{12} = 2.3$, $\chi = 50-100$ cm^{-1}, and $\Gamma = 5-20$ cm^{-1}. The model gave a delocalization size N_{coh} of 4 for both low temperatures and room temperature (*37*, *38*). In this case, the inhomogeneous width is much greater than the homogeneous broadening due to slower exciton relaxation. Consequently, this model predicted slow dynamics of the transient absorption with a time constant of 0.5−1 ps (*37*), whereas the real dynamics are 1 order of magnitude faster. To explain such a fast equilibration, we need higher values of χ and Γ together with smaller σ/V_{12} values.

Alternatively, the absorption line width can be explained using a much smaller value for the disorder ($\sigma/V_{12} \ll 1$) together with introduction of some amount of correlated energy shift or ring deformation, both giving rise to additional splitting between $k = \pm 1$ levels (*48*−*50*). In this case, one should expect a higher degree of delocalization (as compared with the disordered exciton model). Examining these models, we found that they fail to explain the low-temperature fluorescence polarization (*51*) giving a negative polarization in the middle of the band due to the presence of weakly overlapping $k = \pm 1$ levels with perpendicular transition dipoles. These models also cannot explain the dynamics of transient absorption. In the model discussed above, we found that the measured TA dynamics upon blue side excitation reflect a relaxation from the higher $k = \pm 2$ and ± 3 levels down. We also have seen that upon middle-band excitation, corresponding to excitation of the $k = \pm 1$ levels the red shift dynamics are much less pronounced (Figure 5). In the models with elliptical deformation, the absorption spectrum is determined mostly by the $k = \pm 1$ states, whereas the higher exciton states are almost forbidden. In this case, the resulting red shift dynamics upon blue excitation will be very similar to those for middle-band excitation, in disagreement with the experiment. On the other hand, the model of the disordered ring allows us to reproduce the experimental dynamics for various excitation conditions.

Vibrational Coherence

The model discussed above also gives a quantitative explanation for the oscillatory features observed in the TA kinetics for time delays of up to 2 ps (Figure 6). We wish to point out that the "fits" in Figure 6 are the result of a direct calculation of the nonlinear optical response with the same parameters as in Figures 2 and 5. The impulsive excitation

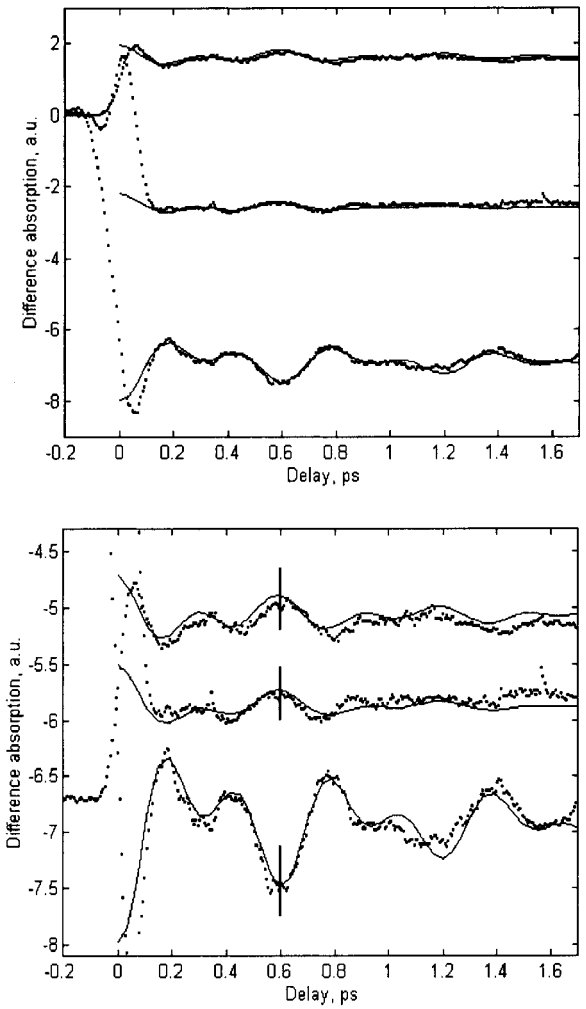

FIGURE 6: Experimental (points) and calculated (solid lines) pump−probe kinetics at 77 K upon excitation at 1055 nm (top frame). Detection wavelengths are as follows (from top to bottom): 1010, 1070, and 1050 nm. Parameters of two vibrational modes: $\Omega_1 = 58$ cm^{-1}, $\Omega_2 = 110$ cm^{-1}, $S_1 = 0.41$, $S_2 = 0.23$, $\gamma_1 = 11$ cm^{-1}, and $\gamma_2 = 11$ cm^{-1}. For the excited state nuclear wave packet, an additional dephasing process was added with a characteristic time constant τ_{hop} of 1.2 ps. The bottom panel shows the same data, but curves are shifted in the vertical direction to make comparison easy.

of electronic levels coupled to specific nuclear modes creates a wave packet in nuclear space (both in the ground state and in the one-exciton manifold). Coherent motion of the ground state wave packet yields oscillations in the photobleaching (PB), whereas the excited state wave packet produces similar oscillations (but with different phase) in the one-exciton stimulated emission (SE) and one- to two-exciton absorption (ESA). Superposition of these three components results in a complicated wavelength-dependent pattern of oscillations in the total TA signal. Fitting these calculated traces to the experimental kinetics yields precise estimates of the frequencies, coupling parameters, and damping constants of the nuclear modes that are involved. We found two main modes with frequencies Ω_1 and Ω_2 of 58 and 110 cm^{-1}, respectively, Huang−Rhys factors S_1 and S_2 of 0.41 and 0.23, respectively, and relaxation constants (rates for the $1 \rightarrow 0$ vibronic transition) γ_1 and γ_2 of 11 cm^{-1} at 77 K. These parameters are slightly dependent on temperature; for example, at 4 K, $\Omega_1 = 65$ cm^{-1}, $\Omega_2 = 101$ cm^{-1}, $S_1 = 0.45$, $S_2 = 0.18$, $\gamma_1 = 7$ cm^{-1}, and $\gamma_2 = 10$ cm^{-1}.

Moreover, it was found that the excited state wave packet required an additional coherence decay with a time constant of ~1.2 ps. This decay can be ascribed to a migration of the localized exciton (polaron) around the ringlike antenna, thereby destroying the vibrational coherence.

Fine Structure of the Absorption Spectrum

In addition to the pronounced oscillations in the time-resolved optical response of LH1 of *Rps. viridis*, there is another consequence of the electron-vibrational coupling; i.e., the linear absorpion spectrum displays fine structure due to the presence of vibrational sublevels associated with the electronic (excitonic) states. This fine structure of the exciton levels together with the exciton splitting itself results in complicated heterogeneous spectra. In Figure 2 (bottom frame), we compare the inverted second-derivative spectrum (SDA) measured for *Rps. viridis* at 4 K with the calculated spectrum. The latter was obtained using the vibrational parameters obtained from the experimental TA kinetics at 4 K: $\Omega_1 = 65$ cm^{-1}, $\Omega_2 = 101$ cm^{-1}, $S_1 = 0.45$, $S_2 = 0.18$, $\gamma_1 = 7$ cm^{-1}, and $\gamma_2 = 10$ cm^{-1}. The homogeneous line broadening due to electronic dephasing and relaxation cannot be calculated using Redfield theory (which is not valid at very low temperatures). We therefore used a more simple model assuming Gaussian line shapes with widths (fwhm) of 4 cm^{-1} for the lowest and 45 cm^{-1} for the higher exciton states. The geometry of LH1 (circular aggregate with 32 molecules) and intermolecular couplings ($V_{12} = 400$ cm^{-1} and $V_{23} = 290$ cm^{-1}) were taken to be the same at 77 and 4 K. The site inhomogeneity (σ) at 4 K was adjusted from the SDA fit and was found to be 380 cm^{-1}.

Note the quantitative agreement between model and experiment. For comparison, the absorption profile of the lowest exciton level ($k = 0$) is shown in the same figure (without inhomogeneous broadening). The most intense peaks at 1049 and 1042 nm correspond to the zero-phonon line {0,0}, and to the first vibronic sublevel of the 65 cm^{-1} mode {1,0}. The next five peaks at 1038, 1035, 1031, 1028/1027.5, and 1024 nm correspond to the {0,1}, {2,0}, {1,1}, {3,0}/{0,2}, and {2,1} vibronic sublevels. The sharp features of the SDA spectrum at 1049 and 1042 nm closely correspond to the vibronic sublevels of the lowest $k = 0$ component. In contrast, the higher $k = \pm 1$ and $k = \pm 2$ exciton levels are broadened due to relaxation, leading to a broad structureless component in the absorption/SDA in the 1024−1036 nm region. The substructure of this broad band is determined by the higher vibronic components of the $k = 0$ level.

Thus, the LH1 antenna of *Rps. viridis* is characterized by a strong coupling to two underdamped low-frequency modes (48−65 and 101−110 cm^{-1}). These modes (or at least the 101−110 cm^{-1} mode) are also present in LH1 of the BChl *a*-containing species; however, for the latter, the coupling to these modes is weaker, and moreover, their dephasing is faster (giving rise to a close to structureless SDA spectrum and weaker pump−probe oscillations). It is also important that the homogeneous line shape for *Rps. viridis* determined by intense vibrational sublevels is very broad and comparable with the inhomogeneous width (which is approximately $\sigma N^{-1/2}$, i.e., 75−80 cm^{-1} at 4 K). This is in contrast with the LH1 of *Rb. sphaeroides* where the absorption of the lowest level is largely determined by inhomogeneous broadening (*67*). As a result, the site-selected emission spectra are strongly dependent on excitation wavelength for *Rb. sphaeroides* (*67*), but almost wavelength-independent for *Rps. viridis* (*77*).

An Intuitive View of Energy Migration in the LH1 and LH2 Rings

On the basis of our modeling of LH1 of *Rps. viridis*, we are in a position to present an intuitive view of energy migration in the LH1 and LH2 rings of photosynthetic purple bacteria.

Ultrafast Exciton Relaxation. Absorption of a light quantum by the LH1 or LH2 antenna creates a superposition of exciton-vibrational states, i.e., a vibrational wave packet in nuclear space (represented by normal coordinates of the relevant nuclear modes) and an exciton wave packet in real space. The latter can be depicted by the density matrix in the site representation (Figure 7), where the diagonal distribution ρ_{nn} corresponds to excitation density of the nth site, while the decay in the antidiagonal direction, $\rho_{n,n+m}$, reflects a coherence between different sites. The inverse participation ratio of the density matrix (*31*) yields the time-dependent degree of delocalization. The initially created wave packet is delocalized over 10−13 molecules. Electronic relaxation in the one-exciton manifold is accompanied by a dynamic localization of the excitation on four to six pigment molecules at room temperature (Figure 7). The steady state excitation density ρ_{nn} is determined by the structure of the lowest exciton levels (for any particular realization of the disorder, as shown in Figure 7). Averaging this result over many realizations would give a uniform diagonal distribution $\rho_{nn}(n)$ with a nonuniform antidiagonal shape $\rho_{n,n+m}(m)$ reflecting the steady state coherence length [for our model, the fwhm of $\rho_{n,n+m}(m)$ (N_{coh}) is 8 at 77 K and 5 at 300 K]. This equilibration of the electronic coordinate is what is observed by the (fluorescence) anisotropy decay and the dynamic Stokes shift of the TA. It should be stressed that these ultrafast phenomena can be quantitatively explained in terms of pure exciton relaxation during the first 100−200 fs after excitation driven by fast fluctuations in the electronic energies and pigment−pigment couplings.

Migration of the Excitation in the Antenna. In the purely excitonic picture, the exciton wave packet is created together with a uniform (site-independent) displacement of the nuclear oscillators. In this case, all one-exciton states have the same oscillator displacement (as shown in Figure 4) and it is reasonable to suppose that the exciton relaxation does not influence the dynamics along the vibrational coordinate. The quality of our modeling of the experimental data demonstrates that this is a good approximation for the real antenna (Figures 5 and 6). The position of the steady state exciton wave packet within a single ring (i.e., for one realization of the static disorder) is determined by the relative phases of the participating exciton states. Any changes in these phases (induced by a weak coupling to the bath) will result in a motion of the wave packet, i.e., some wiggling around the pattern shown in Figure 7. However, this motion cannot be viewed in the density matrix picture (and, therefore, not in any physically measurable quantity such as anisotropy, Stokes shift, etc.), because even for a single realization of

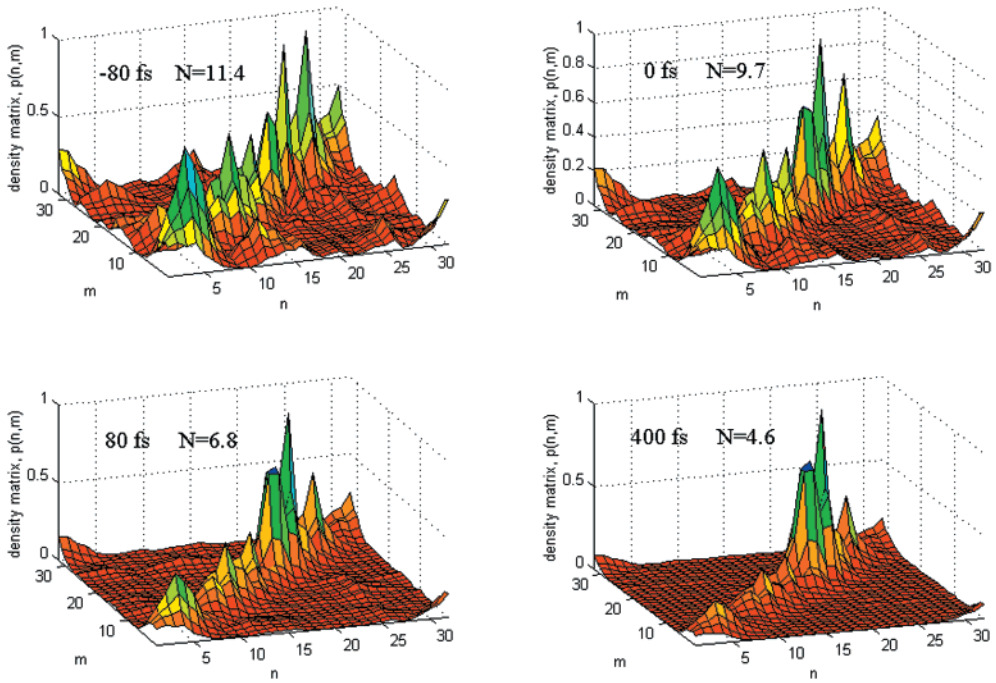

FIGURE 7: Time evolution of the real-space density matrix for LH1 at room temperature calculated for one particular realization of the static disorder. The density matrix $\rho_{n,m}$ is shown at −80, 0, 80, and 400 fs delays (the 400 fs delay corresponds to the steady state limit). The *N* values correspond to a delocalization size calculated as the inverse participation ratio of the density matrix (*31*).

the disorder as shown in Figure 7 the result is averaged over the system−bath interactions.

In this idealized model, we have neglected the effects due to a possible nonuniform displacement of the nuclear oscillators that can be created in the case of strong exciton-vibrational coupling. On its turn, local deformations (in time) may give rise to a more localized exciton (polaron) state. An additional decay component that we detected in the decay of the excited state vibrational coherences can be explained by assuming an (incoherent) migration of the delocalized polaron around the ringlike antenna with a characteristic time constant of ∼1.2 ps at 77 K. The time constant of this decay τ_{hop} is connected with the effective time of migration over a distance comparable with the delocalization length. We note that the estimated hopping constant τ_{hop} of 1.2 ps corresponds to a significant amount of delocalization (remember that N_{coh} = 8 at 77 K). For comparison, if one supposes a fully localized excitation in LH1, then the estimated hopping constant would be less than 100 fs (*15*).

Generally, the self-consistent dynamics of a polaron on a picosecond time scale will be determined by some complicated interplay between the electronic and vibrational coordinates, a feature that is not present in our current model. The relevant coordinates are essentially nonequilibrated on the time scale of polaron migration, so the standard polaron theory (that deals with the lowest polaron band) cannot be used. Although a general physical approach to this problem was developed (*98*), there has been no attempt so far to apply it to the photosynthetic antenna.

Energy Transfer from the Antenna to the RC. Energy trapping by bacterial RCs can be considered as almost single-step hopping from the antenna with a time constant of ∼50 ps (*99*−*101*) with a small probability of back transfer (10−15%; see refs *102*−*105*). Such a transfer is slower than electronic and vibrational equilibration in the antenna and, therefore, can be described by conventional Förster theory. The matrix element connecting the *k*th exciton level of the antenna and the RC's special pair is proportional to the dipole strength of the exciton level, d_k^2, if the special pair is located in the center of the ring (*106*). In this respect, the enhancement of the trapping rate has the same nature as the superradiance of the lowest exciton levels. It is noteworthy that the temperature dependencies of the antenna−RC trapping rate and the antenna superradiance are similar; i.e., both are almost temperature-independent (*34*, *99*). The trapping length (i.e., the increase in trapping rate with respect to a completely localized limit) should be close to the thermally averaged superradiance length. In fact, it is slightly larger (∼5−6) due to a better overlap of the special pair lowest excitonic level with the higher $k = \pm 1$ states of the antenna. Upon the mixture is cooled to ultralow temperatures, the trapping becomes extremely heterogeneous and very dependent on the particular realization of the disorder for each RC−LH1 core (*107*).

From Förster to Redfield Theory

The key parameter that determines the energy transfer and energy relaxation dynamics in these bacterial light-harvesting antenna proteins is the ratio between the exciton coupling V_{12} and energetic disorder σ. In the case of strong coupling ($\sigma/V_{12} \ll 1$), the dynamics include the relaxation between completely delocalized eigenstates that can be described by the master equation for the exciton populations (*108*). In the opposite limit of weak coupling (or strong disorder, $\sigma/V_{12} \gg 1$), excitations are localized on single pigment molecules. The hopping of these localized excitations is given by the master equation in the site representation (*108*). The hopping constant can be obtained using standard Förster theory (*109*) with a possible generalization to the case of "hot transfer" due to slow vibrational relaxation (*110*, *111*). Including the

phase information (coherence terms) in these master equations allows interpolation between the weak and strong coupling limits. For example, the stochastic Liouville equations for the density matrix enabled a smooth transition between these two limits (*108*, *112*). The stochastic model is the high-temperature limit of the more general Redfield approach, i.e., Liouville equations with the Redfield relaxation superoperator added that incorporates the relaxation dynamics between all the elements of the density matrix (either in the site or in the exciton representation) (*113*). The Redfield relaxation tensor can be expressed through the system−bath couplings with arbitrary spectral density (*94*, *95*). In such a model (used in the analysis presented here), no assumptions were made a priori about the degree of exciton delocalization. Instead of describing the system in either the relaxation or hopping limit, we obtain the self-consistent dynamics of the exciton wave packet, which can be viewed as the density matrix evolution in the eigenstate (relaxation) or site representation (hopping).

ACKNOWLEDGMENT

The critical discussions with Dr. Bruno Robert are gratefully acknowledged. We thank Dr. Richard Cogdell for providing us with Figure 1.

REFERENCES

1. Van Grondelle, R., Dekker, J. P., Gillbro, T., and Sundström, V. (1994) *Biochim. Biophys. Acta 1187*, 1−65.
2. Sundström, V., Pullerits, T., and van Grondelle, R. (1999) *J. Phys. Chem. B 103*, 2327−2346.
3. Duysens, L. N. M. (1952) Thesis, State University of Utrecht, Utrecht, The Netherlands.
4. Zuber, H., and Cogdell, R. J. (1995) in *Anoxygenic Photosynthetic Bacteria* (Blankenship, R. E., Madigan, M. T., and Bauer, C. E., Eds.) pp 315−348, Kluwer Academic Publishers, Dordrecht, The Netherlands.
5. Van Grondelle, R. (1985) *Biochim. Biophys Acta 811*, 147−195.
6. McDermott, G., Prince, S. M., Freer, A. A., Hawthornthwaite-Lawless, A. M., Papiz, M. Z., Cogdell, R. J., and Isaacs, N. W. (1995) *Nature 374*, 517−521.
7. Koepke, J., Hu, X., Muenke, C., Schulten, K., and Michel, H. (1996) *Structure 4*, 581−597.
8. Karrasch, S., Bullough, P. A., and Ghosh, R. (1995) *EMBO J. 14*, 631−638.
9. Hu, X., Ritz, T., Damjanovic, A., and Schulten, K. (1997) *J. Phys. Chem. B 101*, 3854−3871.
10. Hu, X., and Schulten, K. (1998) *Biophys. J. 75*, 683−694.
11. Walz, T., Jamieson, S. J., Bowers, C. M., Bullough, P. A., and Hunter, C. N. (1998) *J. Mol. Biol. 282*, 833−845.
12. Ikedayamasaki, I., Odahara, T., Mitsuoka, K., Fujiyoshi, Y., and Murata, K. (1998) *FEBS Lett. 425*, 505−508.
13. Jungas, C., Ranck, J.-L., Rigaud, J.-L., Joliot, P., and Vermeglio, A. (1999) *EMBO J. 18*, 534−542.
14. Frese, R. N., Olsen, J. D., Bränvall, R., Westerhuis, W. H. J., Hunter, C. N., and van Grondelle, R. (2000) *Proc. Natl. Acad. Sci. U.S.A. 97*, 5197−5202.
15. Bradforth, S. E., Jimenez, R., van Mourik, F., van Grondelle, R., and Fleming, G. R. (1995) *J. Phys. Chem. 99*, 16179−16191.
16. Jimenez, R., Dikshit, S. N., Bradforth, S. E., and Fleming, G. R. (1996) *J. Phys. Chem. 100*, 6825−6834.
17. Joo, T., Jia, Y., Yu, J.-Y., Jonas, D. M., and Fleming, G. R. (1996) *J. Phys. Chem. 100*, 2399−2409.
18. Jimenez, R., van Mourik, F., Yu, J. Y., and Fleming, G. R. (1997) *J. Phys. Chem. B 101*, 7350−7359.
19. Kumble, R., Palese, S., Visschers, R. W., Dutton, P. L., and Hochstrasser, R. M. (1996) *Chem. Phys. Lett. 261*, 396−404.
20. Savikhin, S., and Struve, W. S. (1996) *Chem. Phys. 210*, 91−100.
21. Nagarajan, V., Alden, R. G., Williams, J. C., and Parson, W. W. (1996) *Proc. Natl. Acad. Sci. U.S.A. 93*, 13774−13779.
22. Nagarajan, V., Johnson, E. T., Williams, J. C., and Parson, W. W. (1999) *J. Phys. Chem. B 103*, 2297−2309.
23. Koolhaas, M. H. C., van der Zwan, G., Frese, R. N., and van Grondelle, R. (1997) *J. Phys. Chem. B 101*, 7262−7270.
24. Koolhaas, M. H. C., Frese, R. N., Fowler, G. J. S., Bibby, T. S., Georgakopoulou, S., van der Zwan, G., Hunter, C. N., and van Grondelle, R. (1998) *Biochemistry 37*, 4693−4698.
25. Wu, H.-M., Reddy, N. R. S., and Small, G. J. (1997) *J. Phys. Chem. B 101*, 651−656.
26. Wu, H.-M., Rätsep, M., Lee, I.-J., Cogdell, R. J., and Small, G. J. (1997) *J. Phys. Chem. B 101*, 7654−7663.
27. Hu, X., and Schulten, K. (1997) *Phys. Today 50*, 28−34.
28. Hu, X., Damjanovic, A., Ritz, T., and Schulten, K. (1998) *Proc. Natl. Acad. Sci. U.S.A. 95*, 5935−5941.
29. Dracheva, T. V., Novoderezhkin, V. I., and Razjivin, A. P. (1996) *FEBS Lett. 378*, 81−84.
30. Sauer, K., Cogdell, R. J., Prince, S. M., Freer, A., Isaacs, N. W., and Sheer, H. (1996) *Photochem. Photobiol. 64*, 564−576.
31. Meier, T., Chernyak, V., and Mukamel, S. (1997) *J. Phys. Chem. B 101*, 7332−7342.
32. Alden, R. G., Johnson, E., Nagarajan, V., Parson, W. W., Law, C. J., and Cogdell, R. J. (1997) *J. Phys. Chem. B 101*, 4667−4680.
33. Scholes, G. D., Gould, I. R., Cogdell, R. J., and Fleming, G. R. (1999) *J. Phys. Chem. B 103*, 2543−2553.
34. Monshouwer, R., Abrahamsson, M., van Mourik, F., and van Grondelle, R. (1997) *J. Phys. Chem. B 101*, 7241−7248.
35. Kennis, J. T. M., Streltsov, A. M., Vulto, S. I. E., Aartsma, T. J., Nozava, T., and Amesz, J. (1997) *J. Phys. Chem. B 101*, 7827−7834.
36. Kennis, J. T. M., Streltsov, A. M., Permentier, H., Aartsma, T. J., and Amesz, J. (1997) *J. Phys. Chem. B 101*, 8369−8374.
37. Kühn, O., and Sundström, V. (1997) *J. Chem. Phys. 107*, 4154−4164.
38. Chachisvilis, M., Kühn, O., Pullerits, T., and Sundström, V. (1997) *J. Phys. Chem. B 101*, 7275−7283.
39. Monshouwer, R., Baltuška, A., van Mourik, F., and van Grondelle, R. (1998) *J. Phys. Chem. A 102*, 4360−4371.
40. Vulto, S. I. E., Kennis, J. T. M., Streltsov, A. M., Amesz, J., and Aartsma, T. J. (1999) *J. Phys. Chem. B 103*, 878−883.
41. Polívka, T., Pullerits, T., Herek, J. L., and Sundström, V. (2000) *J. Phys. Chem. B 104*, 1088−1096.
42. Book, L. D., Ostafin, A. E., Ponomarenko, N., Norris, J. R., and Scherer, N. F. (2000) *J. Phys. Chem. B 104*, 8295−8307.
43. Novoderezhkin, V., Monshouwer, R., and van Grondelle, R. (1999) *Biophys. J. 77*, 666−681.
44. Novoderezhkin, V., Monshouwer, R., and van Grondelle, R. (1999) *J. Phys. Chem. B 103*, 10540−10548.
45. Scholes, G. D., and Fleming, G. R. (2000) *J. Phys. Chem. B 104*, 1854−1868.
46. Tretiak, S., Middleton, C., Chernyak, V., and Mukamel, S. (2000) *J. Phys. Chem. B 104*, 9540−9553.
47. Novoderezhkin, V., Monshouwer, R., and van Grondelle, R. (2000) *J. Phys. Chem. B 104*, 12056−12071.
48. van Oijen, A. M., Ketelaars, M., Köhler, J., Aartsma, T. J., and Schmidt, J. (1999) *Science 285*, 400−402.
49. Ketelaars, M., van Oijen, A. M., Matsushita, M., Köhler, J., Schmidt, J., and Aartsma, T. J. (2001) *Biophys. J. 80*, 1591−1603.
50. Matsushita, M., Ketelaars, M., van Oijen, A. M., Köhler, J., Aartsma, T. J., and Schmidt, J. (2001) *Biophys. J. 80*, 1604−1614.
51. Wendling, M., Lapouge, K., van Mourik, F., Novoderezhkin, V., Robert, B., and van Grondelle, R. (2001) *Chem. Phys*. (in press).
52. Koolhaas, M. H. C., van der Zwan, G., and van Grondelle, R. (2000) *J. Phys. Chem. B 104*, 4489−4502.

53. Ray, J., and Makri, N. (1999) *J. Phys. Chem. A 103*, 9417−9422.
54. Monshouwer, R., and van Grondelle, R. (1996) *Biochim. Biophys. Acta 1275*, 70−75.
55. Krueger, B. P., Scholes, G. D., and Fleming, G. R. (1998) *J. Phys. Chem. B 102*, 5378−5386.
56. Scholes, G. D., and Fleming, G. R. (2000) *J. Phys. Chem. B 104*, 1854−1868.
57. Kramer, H. J. M., van Grondelle, R., Hunter, C. N., Westerhuis, W. H. J., and Amesz, J. (1984) *Biochim. Biophys. Acta 765*, 156−165.
58. van Amerongen, H., van Haeringen, B., van Gurp, M., and van Grondelle, R. (1991) *Biophys. J. 59*, 992−1001.
59. Hunter, C. N., van Grondelle, R., and Olsen, J. D. (1989) *Trends Biochem. Sci. 14*, 72−75.
60. Visschers, R. W., Chang, M. C., van Mourik, F., Parkes-Loach, P. S., Heller, B. A., Loach, P. A., and van Grondelle, R. (1991) *Biochemistry 30*, 5734−5742.
61. van Mourik, F., van der Oord, J. R., Visscher, K. J., Parkes-Loach, P. S., Loach, P. A., Visschers, R. W., and van Grondelle, R. (1991) *Biochim. Biophys. Acta 1059*, 111−119.
62. Miller, J. F., Hinchigeri, S. B., Parkes-Loach, P. S., Callahan, P. M., Sprinkle, J. R., Riccobono, J. R., and Loach, P. A. (1987) *Biochemistry 26*, 5055−5062.
63. Barz, W. P., Verméglio, A., Francia, F., Venturoli, G., Melandri, B. A., and Oesterhelt, D. (1995) *Biochemistry 34*, 15248−15258.
64. McGlynn, P., Westerhuis, W. H. J., Jones, M. R., and Hunter, C. N. (1996) *J. Biol. Chem. 271*, 3285−3292.
65. Francia, F., Wang, J., Venturoli, G., Melandri, B. A., Barz, W. P., and Oesterhelt, D. (1999) *Biochemistry 38*, 6834−6845.
66. Kramer, J. M., Pennoyer, J. D., van Grondelle, R., Westerhuis, W. H. J., Niederman, R. A., and Amesz, J. (1984) *Biochim. Biophys. Acta 767*, 335−344.
67. van Mourik, F., Visschers, R. W., and van Grondelle, R. (1992) *Chem. Phys. Lett. 193*, 1−7.
68. Visschers, R. W., Germeroth, L., Michel, H., Monshouwer, R., and van Grondelle, R. (1995) *Biochim. Biophys. Acta 1230*, 147−154.
69. Westerhuis, W. H. J., Hunter, C. N., van Grondelle, R., and Niederman, R. A. (1999) *J. Phys. Chem. B 103*, 7733−7742.
70. Reddy, N. R. S., Small, G. J., Seibert, M., and Picorel, R. (1991) *Chem. Phys. Lett. 181*, 391−399.
71. Reddy, N. R. S., Picorel, R., and Small, G. J. (1992) *J. Phys. Chem. 96*, 6458−6464.
72. Reddy, N. R. S., Cogdell, R. J., Zhao, L., and Small, G. J. (1993) *Photochem. Photobiol. 57*, 35−39.
73. Georgakopoulou, S., Frese, R. N., Johnson, E., Koolhaas, M. H. C., Cogdell, R. J., van Grondelle, R., and van der Zwan, G. (2001) *Biophys. J.* (submitted for publication).
74. Dracheva, T. V., Novoderezhkin, V. I., and Razjivin, A. P. (1995) *Chem. Phys. 194*, 223−235.
75. Meier, T., Zhao, Y., Chernyak, V., and Mukamel, S. (1997) *J. Chem. Phys. 107*, 3876−3893.
76. Zhang, W. M., Meier, T., Chernyak, V., and Mukamel, S. (1998) *J. Chem. Phys. 108*, 7763−7774.
77. Monshouwer, R., Visschers, R. W., van Mourik, F., Freiberg, A., and van Grondelle, R. (1995) *Biochim. Biophys. Acta 1229*, 373−380.
78. Zuber, H., and Brunisholz, R. A. (1991) in *Chlorophylls* (Scheer, H., Ed.) pp 627−703, CRC Press, Boca Raton, FL.
79. Visser, H. M., Somsen, O. J. G., van Mourik, F., Lin, S., van Stokkum, I. H. M., and van Grondelle, R. (1995) *Biophys. J. 69*, 1083−1099.
80. Xiao, W., Lin, S., Taguchi, A. K. W., and Woodbury, N. W. (1994) *Biochemistry 33*, 8313−8322.
81. Pullerits, T., Chachisvilis, M., Jones, M. R., Hunter, C. N., and Sundström, V. (1994) *Chem. Phys. Lett. 224*, 355−365.
82. Chachisvilis, M., Pullerits, T., Jones, M. R., Hunter, C. N., and Sundström, V. (1994) *Chem. Phys. Lett. 224*, 345−354.
83. Chachisvilis, M., Fidder, H., Pullerits, T., and Sundström, V. (1995) *J. Raman Spectrosc. 26*, 513−522.
84. Chachisvilis, M., and Sundström, V. (1996) *Chem. Phys. Lett. 261*, 165−174.
85. Salverda, J. M., van Mourik, F., van der Zwan, G., and van Grondelle, R. (2000) *J. Phys. Chem. B 104*, 11395−11408.
86. Yu, J.-Y., Nagasava, Y., van Grondelle, R., and Fleming, G. R. (1997) *Chem. Phys. Lett. 280*, 404−410.
87. Novoderezhkin, V., and van Grondelle, R. (2001) *J. Phys. Chem. B* (submitted for publication).
88. Cherepy, N. J., Du, M., Holzwarth, A. R., and Mathies, R. A. (1996) *J. Phys. Chem. 100*, 4662−4671.
89. Vos, M., Breton, J., and Martin, J.-L. (1997) *J. Phys. Chem. B 101*, 9820−9832.
90. Arnett, D. C., Moser, C. C., Dutton, P. L., and Scherer, N. F. (1999) *J. Phys. Chem. B 103*, 2014−2032.
91. Jean, J. M., and Fleming, G. R. (1995) *J. Chem. Phys. 103*, 2092−2101.
92. Leegwater, J. A. (1995) *J. Phys. Chem. 99*, 11605−11611.
93. Kühn, O., and Sundström, V. (1997) *J. Phys. Chem. B 101*, 3432−3440.
94. Dahlbom, M., Minami, T., Chernyak, V., Pullerits, T., Sundström, V., and Mukamel, S. (2000) *J. Phys. Chem. B 104*, 3976−3983.
95. Chernyak, V., Minami, T., and Mukamel, S. (2000) *J. Chem. Phys. 112*, 7953−7963.
96. Renger, Th., and May, V. (1997) *J. Phys. Chem. B 101*, 7232−7240.
97. Renger, Th., and May, V. (1997) *Photochem. Photobiol. 66* (*5*), 618−627.
98. Chernyak, V., and Mukamel, S. (1996) *J. Chem. Phys. 105*, 4565−4583.
99. Visscher, K. J., Bergström, H., Sundström, V., Hunter, C. N., and van Grondelle, R. (1989) *Photosynth. Res. 22*, 211−217.
100. Bergström, H., van Grondelle, R., and Sundström, V. (1989) *FEBS Lett. 250*, 503−508.
101. Beekman, L. M. P., van Mourik, F., Jones, M. R., Visser, H. M., Hunter, C. N., and van Grondelle, R. (1994) *Biochemistry 33*, 3143−3147.
102. Abdourakhmanov, I. A., Danielius, R., and Razjivin, A. P. (1989) *FEBS Lett. 245*, 47−50.
103. Timpmann, K., Zhang, F. G., Freiberg, A., and Sundstrom, V. (1993) *Biochim. Biophys. Acta 1183*, 185−193.
104. Otte, S. C. M., Kleinherenbrink, F. A. M., and Amesz, J. (1993) *Biochim. Biophys. Acta 1143*, 84−90.
105. Somsen, O. J. G., van Grondelle, R., and Valkunas, L. (1996) *Biophys. J. 70*, 669−683.
106. Novoderezhkin, V. I., and Razjivin, A. P. (1994) *Photosynth. Res. 42*, 9−15.
107. Somsen, O. J. G., van Grondelle, R., and Valkunas, L. (1994) *Biophys. J. 66*, 1580−1596.
108. Rahman, T. S., Kenkre, V. M., and Knox, R. S. (1979) *Chem. Phys. 44*, 197−211.
109. Förster, T. (1965) in *Modern Quantum Chemistry. Istanbul Lectures. Part III: Action of Light and Organic Crystals* (Sinannoglu, O., Ed.) pp 93−137, Academic Press, New York.
110. Tehver, I., and Hizhnyakov, V. (1974) *ZETF Lett. 19*, 338−342.
111. Kenkre, V. M. (1977) *Phys. Rev. A 16*, 766−776.
112. Knox, R. S., and Gülen, D. (1993) *Photochem. Photobiol. 57*, 40−43.
113. Redfield, A. G. (1965) *Adv. Magn. Reson. 1*, 1−32.

BI011398U